PCCP

Shells in CO2 clusters

Journal:	*Physical Chemistry Chemical Physics*
Manuscript ID	CP-ART-12-2021-005866.R1
Article Type:	Paper
Date Submitted by the Author:	04-Feb-2022
Complete List of Authors:	Niman, John; University of Southern California, Physics and Astronomy Kamerin, Benjamin; University of Southern California, Physics and Astronomy Kresin, Vitaly; University of Southern California, Physics and Astronomy Krohn, Jan; ETH Zurich, Laboratory for Physical Chemistry Signorell, Ruth; ETH Zürich, Department of Chemistry and Applied Biosciences Halonen, Roope; Tianjin University, Center of Joint Quantum Studies, School of Science Hansen, Klavs; Tianjin University, Center of Joint Quantum Studies, School of Science; Lanzhou University, Lanzhou Center for Theoretical Physics, Key Laboratory of Theoretical Physics of Gansu Province

PCCP

ARTICLE TYPE

Cite this: DOI: 00.0000/xxxxxxxxxx

Shells in CO_2 clusters†

John W. Niman,[a] Benjamin S. Kamerin,[a] Vitaly V. Kresin,[a] Jan Krohn,[b] Ruth Signorell,[b] Roope Halonen,[c] and Klavs Hansen*[c,d]

Received Date
Accepted Date

DOI: 00.0000/xxxxxxxxxx

Abundance spectra of $(CO_2)_N$ clusters up to $N \approx 500$ acquired under a wide range of adiabatic expansion conditions are analyzed within the evaporative ensemble framework. The analysis reveals that the cluster stability functions display a strikingly universal pattern for all expansion conditions. These patterns reflect the inherent properties of individual clusters. From this analysis the size-dependent cluster binding energies are determined, shell and subshell closing sizes are identified, and cuboctahedral packing ordering for sizes above $N \approx 130$ is confirmed. It is demonstrated that a few percent variation in the dissociation energies translates into significant abundance variations, especially for the larger clusters.

1 Introduction

One of the most striking phenomena associated with clusters is the strong non-monotonic variation of their properties with size. Such finite size effects have been observed in a number of different types of clusters, composed by materials as diverse as atoms of noble gases[1] or simple metals[2,3], as well as in the all-carbon fullerenes[4]. The variations reflect the shell structure of the clusters, which can be of electronic nature[2,5] or arising out of the packing of atoms[1,6].

The shell structures in these systems were discovered in molecular beams, manifested in the highly irregular variation of the abundances with cluster size. Shell structure appears in mass abundance spectra because the size-to-size intensity variations reflect the cluster binding energies. The connection between cluster stabilities (*i.e.*, binding energies) and their abundances is, however, not elementary, and cannot be understood as simple equilibrium distributions with the temperature set by the source temperature. In many cases involving cluster beams one finds that the underlying process that shapes the size-to-size abundance variations is that of evaporative cascades: internally excited (hot) clusters undergo a series of evaporation steps resulting in a detected population where the high cluster intensities reflect lower than average evaporation rates and vice versa. The high intensity clusters, often labeled "magic numbers," are frequently assigned a special stability. This is, however, a simplified view that will only hold in special situations, as the general theory below shows, and this must be taken into account in the quantitative analysis of cluster binding energies extracted from such spectra.

Importantly, just a few evaporative steps are sufficient for the population patterns to acquire the shapes that characterize the species[7,8]. These shapes make it possible to use measurements of relative abundances to extract quantitative information about the monomer-by-monomer variations of cluster binding energies with size. The connection between abundances and binding energies was derived in Ref. 8 and is discussed at length in Ref. 9. It has been applied previously to analyze mass spectra of sodium clusters[10], for which a dedicated experiment unambiguously confirmed the shell energy amplitudes derived from the abundance spectra[11]. It has also been used for clusters of both light and heavy water[12,13], quantifying in particular the excess stability of the $N = 21$ protonated cluster that gives rise to the well-known abundance peak at that size. Finally, it was applied to find the energy amplitudes of the packing shells which shape the rare gas cluster mass spectra[14].

This work applies the analysis to a large number of abundance spectra of CO_2 clusters. The experiments were performed to study nucleation in supersaturated gases[15], but are equally useful for the analysis here, in particular because the wide range of nucleation and detection conditions employed in the measurements offers an uncommonly rich data set. We will demonstrate that the analysis of the mass spectra reveals that highly universal patterns are present in all observed distributions. The derived stabilities are assigned to the neutral clusters produced in the beam.

The plan of the remainder of the paper is as follows. First a

[a] *Department of Physics and Astronomy, University of Southern California, Los Angeles, California 90089-0484, USA.*
[b] *Laboratory of Physical Chemistry, ETH Zürich, Vladimir-Prelog Weg 2, CH-8093 Zürich, Switzerland.*
[c] *Center for Joint Quantum Studies and Department of Physics, School of Science, Tianjin University, 92 Weijin Road, Tianjin 300072, China.*
[d] *Lanzhou Center for Theoretical Physics, Key Laboratory of Theoretical Physics of Gansu Province, School of Physical Science and Technology, Lanzhou University, Lanzhou 730000, China. E-mail: klavshansen@tju.edu.cn. Homepage: http://www.klavshansen.cn/*

† Electronic Supplementary Information (ESI) available. See DOI: 10.1039/cXCP00000x/

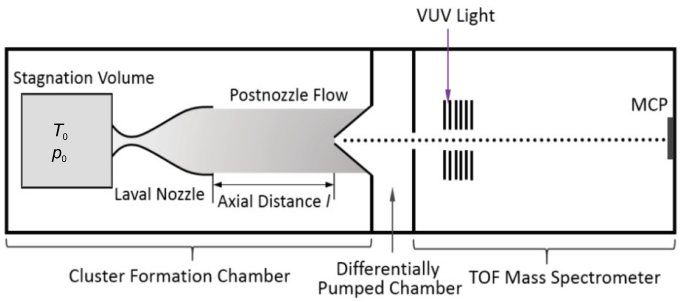

Fig. 1 Outline of the experimental setup. Clusters were generated by the expansion of a mixture of CO_2 and argon as a cooling gas, photoionized, and detected by a time-of-flight mass spectrometer, as described in the text. Figure adapted from Fig. 1 of Ref. 19 with permission from the PCCP Owner Societies.

brief description of the experimental procedure is given. Then the theory of the formation of the abundance spectra and the analysis are described. Next the dissociation energies extracted from the analysis are given, followed by a section where these values are discussed in terms of packing shell structure. The results are discussed and summarized in the concluding section.

2 Experimental procedure and results

The experimental equipment has been described in detail in Ref. 16 where it was employed for nucleation studies[15–17], and only a brief summary is given here.

Figure 1 shows a schematic drawing of the setup. Clusters were produced by co-expansion of CO_2 with argon, which acted as a carrier gas, through a pulsed Laval nozzle with a throat diameter of 4.1 mm. The gas expanded from a stagnation pressure of $p_0 \approx 8 \times 10^4$ Pa and room temperature. The CO_2 mole fraction before expansion was varied between 0.38 % and 5.02 %.

At a distance ℓ after the nozzle, the core of the expansion was sampled with a skimmer and the clusters were single-photon ionized by 13.8 eV (89.8 nm) photons generated with a home-built tabletop vacuum ultraviolet (VUV) laser. The laser operates with 2-color-4-wave mixing in an expanding krypton gas at a repetition rate of 20 Hz. By varying the distance between the nozzle exit and the skimmer, the beam could be sampled at different times in the post-nozzle flow. After ionization the clusters were were accelerated to 30 keV and the mass spectra were measured in a linear time-of-flight mass spectrometer (TOFMS) equipped with a microchannel plate (MCP) detector. The resolution of the TOFMS was 800 at $m/z = 12000$ u. No sign of multiply charged clusters were observed in the relevant size range. The appearance size for doubly charged clusters is $N = 44$[18] and if they had been present odd-numbered cluster sizes would have been easily seen as nominally half-integer mass peaks.

Figure 2 shows three examples of mass spectra recorded with different CO_2 mole fractions and nozzle-TOFMS separations. These mass spectra were obtained from the raw time-of-flight data by applying background subtraction and rescaling, as described in the Electronic Supplementary Information (ESI). The variation of the average cluster size with source parameters is discussed in Ref. 15, and since average sizes are not relevant for the analysis here, we will refrain from a detailed description of this aspect.

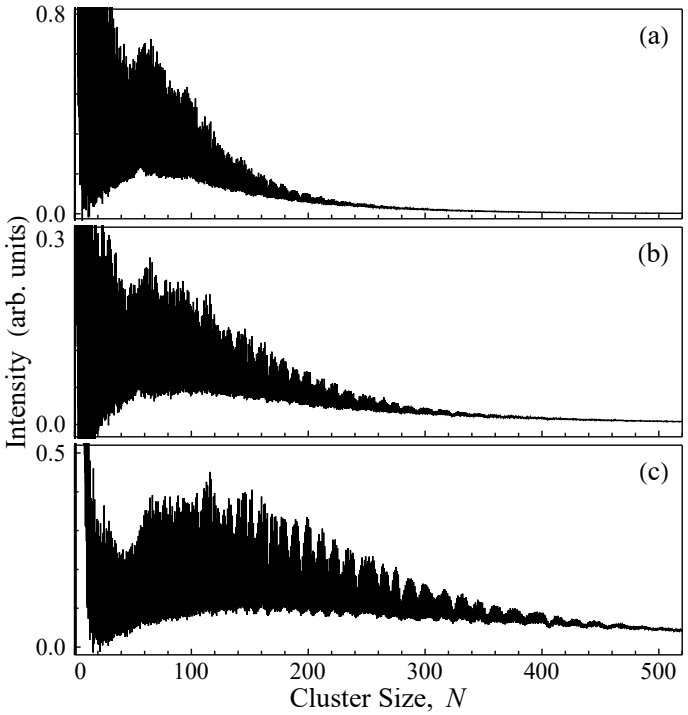

Fig. 2 Three representative cluster mass spectra with different CO_2-argon mixtures and nozzle-TOFMS separations: (a) 1.54 % CO_2 mole fraction and 323 mm nozzle-ionization distance, (b) 1.54 % CO_2 and 403 mm distance, (c) 3.85 % CO_2 and 403 mm distance. Spectra are reproduced from data reported in Ref. 15.

The $(CO_2)_N^+$ distributions show a clearly visible structure with periodic intensity modulations with a period on the order of 10 monomers. The pattern seen in the figure is reproducible for clusters larger than approximately 130 molecules. It has been observed previously[15,20] and ascribed to shell closings in cuboctahedral cluster structures. Similar variations have been seen in anionic clusters[21]. In the present paper the focus is on the important information about cluster structure and in particular about the magnitude of the underlying stability variations that can be extracted from these persistent patterns.

3 Data analysis

The minima in the mass spectra, $N_{\min}$, are well defined, and for a first approximate picture of the stability pattern the cube roots of their positions are plotted vs. their number of appearance. Such plots are shown in Fig. 3 for the three spectra shown in Fig. 2 (integrated as described below). The nearly equidistant spacing, here with approximately ten dips for each unity increment of $N_{\min}^{1/3}$, is a signature of shell structure[6]. The numerical value of the spacing indicates that the structure is face centered cubic, either cuboctahedral (truncated *fcc*), as already suggested in Ref. 20, or distorted (octahedral) *fcc*[22].

After confirming the assignment of the intensity variations to shell structure, two questions arise. First, one may inquire about the precise *location* of the shells (or subshells), because these are almost certainly not coincident with the abundance spectra min-

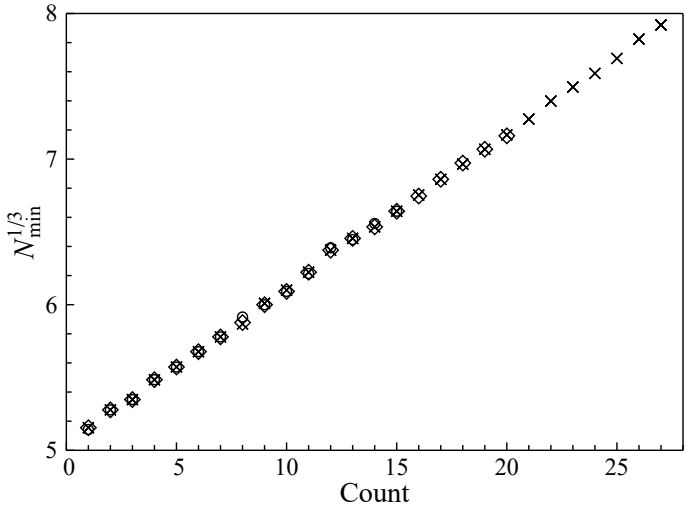

Fig. 3 The cube root of cluster sizes $N_{\min}$ corresponding to abundance minima, plotted in the order of their appearance in the abundance spectra of Fig. 4 below. Circles, squares, and crosses correspond to spectra labeled (a), (b), and (c), respectively. The count included in this plot starts at $N_{\min} = 130$.

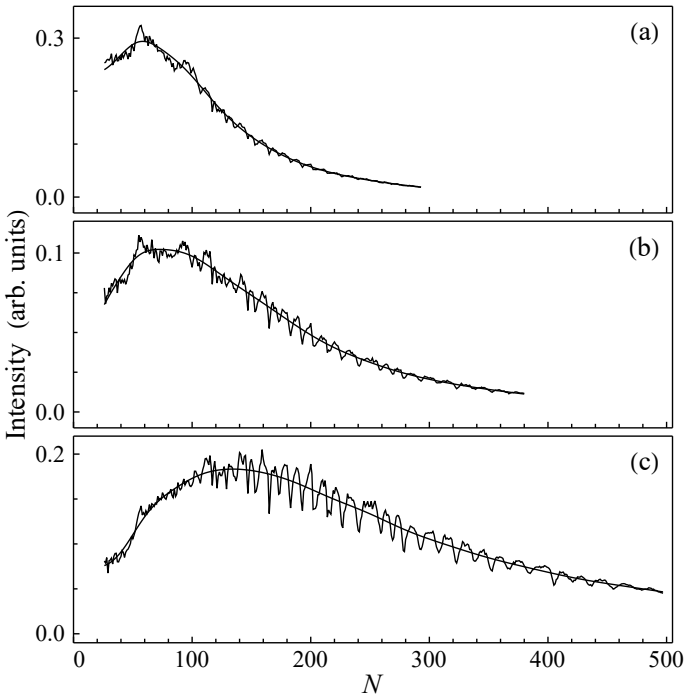

Fig. 4 Integrated abundance spectra I_N derived from the mass spectra in Fig. 2, and their smooth envelope functions $\tilde{I}_N$.

ima. The second question concerns the *energy amplitude* of the shell modulation that is manifested in the abundance spectra. Both of these questions will be answered by application of the theory mentioned in the Introduction and given in detail in Refs. 8 and 9.

The analysis of the mass spectra begins with an integration of the individual mass peaks. As described in detail in the ESI, this involves identifying and subtracting a constant baseline and incorporating a smooth correction for the mass scaling and photoionization efficiency. Following these steps, the midpoints between mass peaks are identified and the intensity between these is integrated. This yields the ion intensities I_N as a function of cluster size N.

Spectra recorded under different source conditions are made up of a smooth envelope function modulated by the abundance variations. The latter are shaped by the evaporative losses and carry the information that is of interest here. The smooth envelope function, in contrast, is shaped by the precise parameters of the cluster source. In order to extract the evaporative abundance variations from the spectra recorded under different source conditions, the envelope function is determined for each spectrum and divided out. These envelope functions, denoted $\tilde{I}_N$, were calculated by iterative convolution of the integrated mass spectra with Gaussian functions,

$$\tilde{I}_N = \frac{\sum_{N'} I_{N'} \exp\left(-(N-N')^2/2w_N^2\right)}{\sum_{N'} \exp\left(-(N-N')^2/2w_N^2\right)}, \qquad (1)$$

where $w_N = 4N^{1/3}$. This is described in more detail in the ESI. Examples of the resulting envelope functions are shown in Fig. 4, plotted together with the individual peak intensities.

After division of the intensity spectra by $\tilde{I}_N$, the thus normalized abundance variation ratios $I_N/\tilde{I}_N$, referred to as stability functions, oscillate around unity. The outcome of this analysis for the three sample spectra from Figs. 2 and 4 with their own envelope functions is shown in Fig. 5, together with the mean stability function of all experimental spectra.

Strikingly, the stability functions derived from all the mass spectra are practically identical in their overlapping regions for values above $N \approx 130$. The good agreement between stability functions extracted from mass spectra produced under a range of different conditions allows us to conclude that they reflect inherent cluster properties, consistent with the hypothesis that they are shaped by evaporative events after production. In contrast, the envelope functions differ widely for different source conditions, as expected from the correspondingly different nucleation parameters [15,23]. Indeed, although it cannot be excluded that clusters may undergo some additional collisions even in the post-skimmer collimated flow, strong size-to-size intensity oscillations are a hallmark outcome of evaporative processes.

The next step in the analysis is to relate the stability function, $I_N/\tilde{I}_N$, to the cluster energies. The function is shaped by the clusters' evaporative activation energies, D_N, which are the main determining factors for the speed of evaporation that can have a non-monotonic size-to-size variation. They can be taken to be identical to the cluster dissociation energies. This identification holds for a molecule-cluster potential without any barrier to attachment, which can be safely assumed for CO_2.

As mentioned above, the number of molecules which is required to have evaporated in order to apply the analysis is small. For the present systems a few evaporative steps suffice [8]. This means, in particular, that conclusions about nucleation [15] drawn from the data are not in any conflict with the present analysis and vice versa.

The analysis in Ref. 8 established the following relation be-

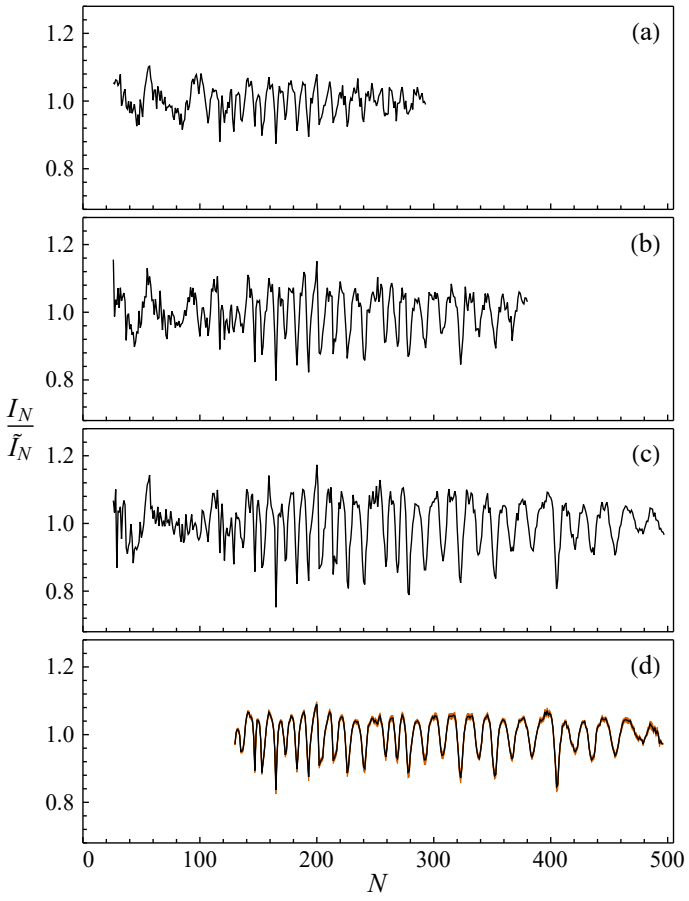

Fig. 5 Top three panels (a–c): stability functions of the three spectra shown in Fig. 4. Bottom panel (d): the average stability function derived from all the mass spectra in the experimental data set (black line) with the standard error of the mean indicated by a brown field.

tween the stability functions and cluster dissociation energies:

$$\frac{I_N}{\tilde{I}_N} = \frac{D_N + D_{N+1}}{2\tilde{D}_N} + \frac{C_N}{\ln(\omega_N t)} \frac{D_N - D_{N+1}}{\tilde{D}_N}. \quad (2)$$

Here $\tilde{D}_N$ is the part of the dissociation energy which varies smoothly with cluster size. It is analogous to the energy of Thomson's drop model[9] and to the liquid drop part of nuclear[24,25] and metal cluster[26–28] binding energies. It should be emphasized that in spite of the name, the applicability of such parametrization is not restricted to liquid phase particles: the essential point is that the energy has a smoothly varying size dependence. C_N is the vibrational heat capacity of the cluster (in units of k_B) for which the bulk heat capacity of solid CO_2, scaled to the cluster size N, is used. Additional small corrections for the microcanonical nature of the process[29] and the overall translational and rotational degrees of freedom are included (see the ESI for details).

The quantity $G_N = \ln(\omega_N t)$ is referred to as the Gspann parameter[30,31]. Here t is the time elapsed between the production of the clusters and the completion of the mass selection in the acceleration stage of the TOFMS. The factor ω_N is the frequency prefactor in the expression for the unimolecular rate constant that describes the statistical process of monomer loss from the clusters. Its value can be estimated from molecular properties, but a simpler procedure is to extract it from the bulk vapor pressure together with the molecular area from the measured bulk density. The procedure is described in detail in the ESI. For the cluster sizes studied here, G_N is found to vary between 32 and 35.

With these two parameters known, the difference equation Eq. (2) can be solved numerically. We rewrite it, ignoring the small difference between $\tilde{D}_N$ and $\tilde{D}_{N+1}$, as

$$\frac{D_N}{\tilde{D}_N} = \frac{1}{\frac{C_N}{G_N} + \frac{1}{2}} \left[\frac{I_N}{\tilde{I}_N} + \frac{D_{N+1}}{\tilde{D}_{N+1}} \left(\frac{C_N}{G_N} - \frac{1}{2} \right) \right], \quad (3)$$

and solve this iteratively. The value of $D_N/\tilde{D}_N$ for the largest size in a spectrum is required as input. Regardless of the precise value of this starting value, the procedure converges to a stable set of dissociation energies for lower N. However, the speed of convergence depends on the chosen starting value. To optimize the convergence speed we varied this value by minimizing the deviation from unity of the resulting set of solutions for all sizes N, as described in the ESI. In all cases these optimized values were consistent with values extracted from the procedure applied to other spectra in overlapping mass regions, confirming the soundness of the procedure.

4 Dissociation energies

The ratios $D_N/\tilde{D}_N$ derived from the spectra in Fig. 5 are displayed in Fig. 6(a–c), and Fig. 6(d) shows the average of all spectra. The variations of the $D_N/\tilde{D}$ values follow those of the stability functions with some important differences.

First of all, the amplitudes of the dissociation energy variations are much smaller than those of the stability functions, due to the large heat capacity factor multiplying the energy differences. This will amplify measured abundance variations very strongly, and more so the larger the clusters. The effect is known and has been observed previously (see Ref. 32 for an extreme case of this amplification). Conversely, this means that when clusters of different sizes are observed to display abundance variations of a similar magnitude, the underlying energy variations are actually larger for the smaller clusters. This is a direct consequence of the above equations but is worth highlighting.

The second important difference is that the maxima and minima of the structure function curves and the energy curves are shifted relative to each other. This is likewise a consequence of the fact that the second term in Eq. (2) is much larger than the first, and that high abundances therefore occur where the dissociation energy *experiences a drop with increasing size* and *not* where it is high.

It is useful to convert the results to absolute energies. This is done by multiplication with the Thomson liquid drop energies, determined by bulk parameters as

$$\tilde{D}_N = A - \frac{2}{3} B N^{-1/3}, \quad (4)$$

where A is the bulk binding energy per molecule, and B is related to the surface tension, γ, via

$$B N^{2/3} = 4\pi r_0^2 N^{2/3} \gamma, \quad (5)$$

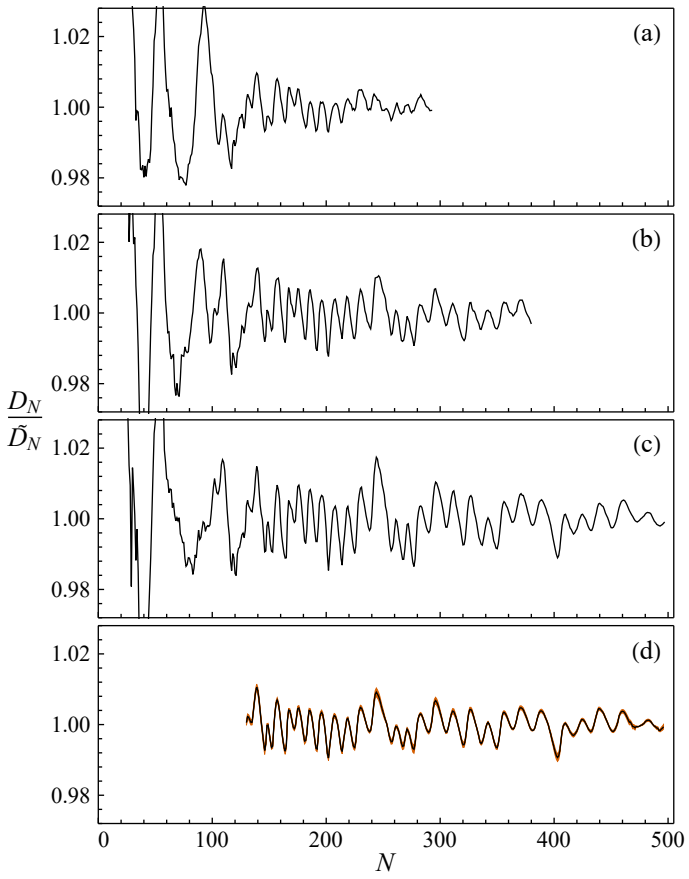

Fig. 6 Top three panels (a–c): dissociation energy ratios calculated from the stability functions in Fig. 5(a–c). Bottom panel (d): dissociation energies averaged over the full data set (black line) with the standard error of the mean given by the brown field. Note the large difference between the scales of the variation of the stability functions and the dissociation energies. This is due to the large value of the ratio C_N/G_N for these cluster sizes.

where r_0 is the molecular averaged radius, defined by the density.

The experimental enthalpy of sublimation[33], 27.2 ± 0.4 kJ/mol (0.28 eV), is used for the value of A. This is not precisely the same quantity as A, but the difference involves only a small difference of thermal energies which can be ignored for the present purpose. The value is close to the one found theoretically in Ref. 23 where macroscopic parameters were used to adjust the interaction potentials and simulations were performed for finite excitation energy clusters in similar size ranges.

No reliable data have been found for the surface energy of solid CO_2, and we will use the relation

$$B = \frac{2}{3}A = 0.188 \text{ eV}, \tag{6}$$

which has been found to give fair estimates for a number of substances, including van der Waals bound solids[9]. The 0 K value derived from Ref. 23 is closer to $B \approx A$. The difference in the cluster dissociation energies between these two variants amounts to a shift downward of about 0.01 eV with very little effect on the relative variations, and can be ignored without any major loss of precision. The dissociation energies calculated from the results in Fig. 6(d) by using these parameters are shown in Fig. 7.

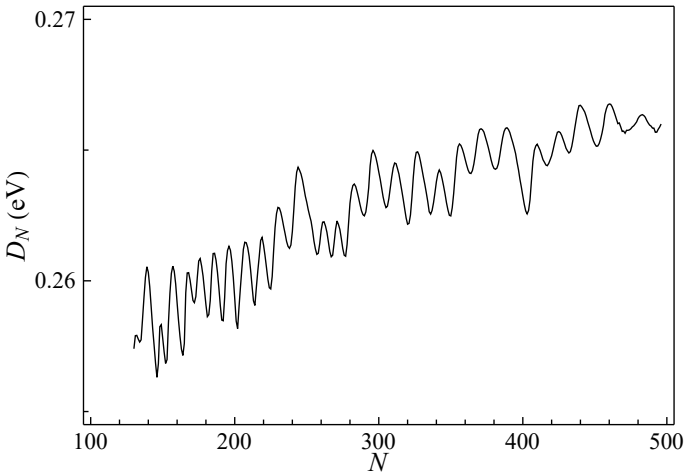

Fig. 7 Cluster dissociation energies calculated from the ratios shown in Fig. 6(d) by using Eq. (4) for $\tilde{D}_N$.

5 Shell structure

As emphasized above, the positions of shell closings do not coincide with the abundance (I_N) maxima. They also are not necessarily given by the maxima in the dissociation energies, D_N, at least at finite temperatures where shell closings tend to spread out over more sizes with increasing amount of thermal excitations. From experimental results on the shell structure of sodium clusters[11] it was concluded that at finite temperatures the shell structure's prototypical sawtooth variation of dissociation energies with cluster size becomes rounded, and the location of shell closings in the presence of such rounding can be identified with the point of steepest descent in the curve of $D_N/\tilde{D}_N$ vs. N. A discussion of this question, applied to experiments on clusters of rare gas atoms, can also be found in Ref. 34. We will likewise identify the steepest slope with the shell closing.

The sequence of shell and subshell closings of $(CO_2)_{N\gtrsim 130}$ clusters is determined according to this prescription from the data in Fig. 6(d). Details of the numerical procedure are described in the ESI. The order of occurrence of subshell closings is quantified with subshell closing index $k' = Fk$, where F is the number of facets on a cluster of k shells. This subshell index k' accounts for individual facets between closed shells given by the index k. The subshell indices for the obtained closings are tentatively assigned by associating the observed closing at $N_s = 143$ with the ideal cuboctahedral cluster of $k = 4$ (*i.e.*, $N = 147$) with index $k' = 14 \times 4 = 56$ illustrated in Fig. 8(a). As shown in Fig. 9, the cube roots of N_s lie on a straight line when plotted against the assigned k'. It is worth pointing out that this identification of the shells structure is more precise and rigorous than the approximate one based on abundance minima illustrated in Fig. 3. The obtained slope of the $N_s^{1/3}$ vs. k' curve, 0.1060 ± 0.0002, is in good agreement with the coefficient for cuboctahedral filling of k' subshells (see the ESI and Refs. 20 and 35 for a detailed description of these subshell closings):

$$N_s^{1/3} \approx 0.1067(k' - 7) \tag{7}$$

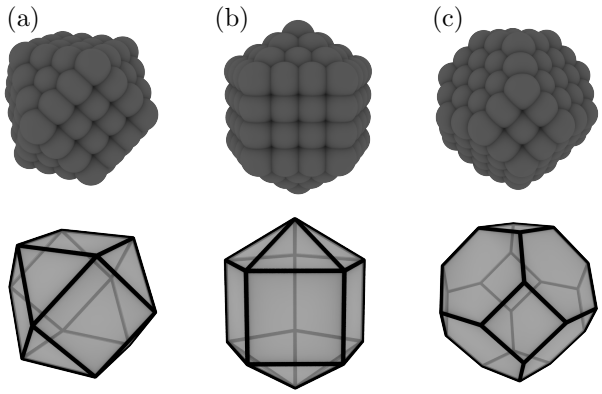

Fig. 8 Shell closings for (a) cuboctahedron with 14 facets ($k=4$, $N=147$), (b) regular Ino decahedron with 15 facets ($k=4$, $N=147$), and (c) truncated octahedron with 14 facets ($k=3$, $N=201$). Detailed discussion and analysis about the geometries of these structures and their (sub)shell closings is given in the ESI.

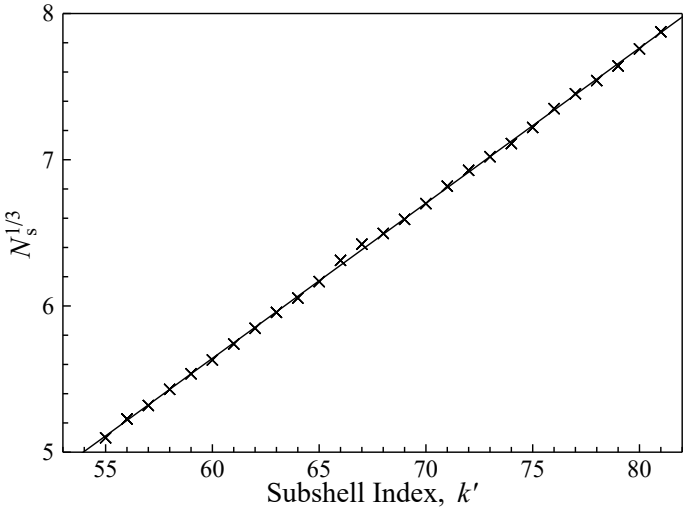

Fig. 9 The cube roots of cluster sizes N_s corresponding to subshell closings, determined from the plot in Fig. 6(d) as described in the text.

Using Eq. (7) as the regression equation also minimizes the y-axis intercept ($N_s^{1/3} = 0.1060(k'-7)+0.028$). This result further supports the aforementioned assignment of the subshell closings according to a cuboctahedral cluster.

The very good agreement of the positions of the subshell closings with those predicted by cuboctahedral structures notwithstanding, it is still of interest to compare the data with alternative structures. In the previous structural analysis by Negishi *et al.* [20], *fcc* cubic, octahedral and icosahedral geometries were included in addition to cuboctahedron. From this set of different structures it is clear that only a cuboctahedral geometry is able to capture the observed $N_s^{1/3}$ vs. k' behavior of CO_2 clusters. However, their analysis ignored structures such as Ino (or Marks) decahedra and truncated octahedra illustrated in Figs. 8(b) and 8(c), respectively. These are generally plausible alternatives for larger clusters[36–39]. For this reason we extended the geometric analysis by Negishi *et al.* [20] (and Näher *et al.* [40]) to truncated octahedral and Ino decahedral clusters. The slopes of the $N_s^{1/3}$ vs. k' curves are expected to be 0.100 for the Ino decahedra and 0.110 for the truncated octahedra, which are substantially closer to the cuboctahedral value than any other structure considered by Negishi *et al.* [20]. To show the general applicability of the used structure identification via cluster energy variations, we have carried out test calculations based on a peeling-off process of the least bound monomers. In short, these calculations fully support the adequacy of the geometric analysis of cluster packing used here and in previous studies. The procedure and the obtained results are discussed in detail in the ESI. The conclusion is that the two alternative structures both give a clearly worse fit of slope of the experimental data, and that the presented sequence of shell closings of CO_2 is best characterized by the cuboctahedral geometry.

6 Summary and discussion

It is a key result of this work that the systematic inversion procedure described in Sec. 3, developed on the basis of evaporative dynamics, makes it possible to identify universal underlying patterns and extract intrinsic cluster parameters from $(CO_2)_N$ abundance data acquired under a wide range of generation conditions.

In particular, the cluster stability functions and dissociation energies derived from different mass spectra are all in close agreement above $N \approx 130$, independent of the precise source position and nozzle expansion conditions. This confirms the underlying physical assumption that the size-to-size variations in the present mass abundance spectra represent the outcome of clusters undergoing several in-flight evaporation steps.

The analysis presented in this work allowed us to determine accurate size-to-size relative variations of the cluster binding energies, to estimate their absolute magnitude, and to identify the sizes of especially stable clusters. The sequence of these sizes, *i.e.*, the shell and subshell closings, confirms the geometrical nature of $(CO_2)_N$ cluster packing, with a cuboctahedral character for $N \gtrsim 130$. This is consistent with the *fcc* bulk structure (see, *e.g.*, Ref. 15 and references therein), and with electron scattering experiments on neutral CO_2 clusters[41].

Implicit in the foregoing discussion has been the assumption that the shell structure and stabilities deduced from the data are characteristic of the neutral rather than cationic CO_2 clusters. In other words, the abundance variations primarily derive from cluster evaporation which happens *en route* from the nozzle to the TOFMS rather than post-ionization. This is consistent with the observation[42] that CO_2 clusters require more than a few microseconds after (electron-impact) ionization to evaporate, which exceeds their residence time within the TOFMS extraction region. Furthermore, abundance modulations observed in beams of $(CO_2)_N^-$ clusters produced by low-energy electron attachment[20,22] have periodicities similar to those detected here in the mass spectra of $(CO_2)_N^+$ clusters[15], which suggests that a charge is in any case of minor importance. It should also be mentioned that contribution to dissociation energies from a Coulomb term is practically negligible outside the low-N range, partly because of the suppression by its size dependence ($\propto N^{-4/3}$) and partly due to the relatively low polarizability of the (non-polar)

CO_2 molecules.

One observation worth pointing out here is the slow decrease of the amplitude in the variations of the *D*'s with size. This suggests that these variations are caused by evaporations from edges and can be summarized as a nearest neighbor effect. This in turn suggests that although the observed structures in the spectra are generated by evaporative processes, these occur from solid clusters, at least in the final step(s). This is consistent with the bulk phase diagram where no liquid phase is present at low pressures and temperatures.

It is not surprising but perhaps still worth mentioning that the elemental composition of the molecules is not a determining factor for the structure, as can be seen by comparison with the structure of CO observed in Ref. 43.

The structure of CO_2 clusters of sizes below 130 remains an interesting open question. Even below the clear onset of cuboctahedral ordering above $N \approx 130$ there is also a notable degree of structure. However, some features appear to evolve gradually with the nozzle expansion parameters (see the ESI), suggesting the presence of structural and phase transformations in this range[44]. In Ref. 20 the cuboctahedral structures were assigned to clusters above $N = 80$. Those clusters were anionic and the difference from our observed lower threshold, maybe due to this difference in the charge state. Interestingly, electron diffraction studies of neutral clusters[41] showed a cubic structure down to $N = 100$, a limit defined by the instrumental resolution, in agreement with the mass spectrometric results for both negatively and positively charged clusters. The precise shell closings were not possible to determine in these studies, unfortunately. The combined experimental and theoretical study in Ref. 44 suggested a somewhat mixed picture with both icosahedral and cubic elements in $N \leq 100$ neutral clusters. A numerical molecular dynamics study[45], also on neutral clusters, indicated the potential existence of a metastable icosahedral structure and a stable *fcc* structure over a range of sizes below 100. Adding to this already mixed picture is the observation that for clusters of sizes 50–70, the shell structure seen in the mass abundance spectra was shown to develop on the time scales of the mass spectrometer flight times[42]. Thus identification of shapes and phases of CO_2 clusters in this size region requires more study.

Conflicts of interest

There are no conflicts to declare.

Acknowledgements

This work was supported by The National Science Foundation of China with grant No. 12047501 and the 111 Project under Grant No. B20063 (R.H.,K.H.), the U.S. National Science Foundation under Grant No. CHE-1664601 (B.S.K., V.V.K, J.W.N.), and by the Swiss National Science Foundation Grant No. 200020_200306 (J.K., R.S.). We thank G.-L. Hou for discussions initiating this work. The figures for this article have been created using the SciDraw scientific figure preparation system 46.

References

1 O. Echt, K. Sattler and E. Recknagel, *Phys. Rev. Lett.*, 1981, **47**, 1121–1124.

2 W. D. Knight, K. Clemenger, W. A. de Heer, W. A. Saunders, M. Y. Chou and M. L. Cohen, *Phys. Rev. Lett.*, 1984, **52**, 2141–2143.

3 W. A. de Heer, W. Knight, M. Chou and M. L. Cohen, in *Solid State Physics*, ed. H. Ehrenreich and D. Turnbull, Academic, New York, 1987, vol. 40, pp. 93–181.

4 H. W. Kroto, J. R. Heath, S. C. O'Brien, R. F. Curl and R. E. Smalley, *Nature*, 1985, **318**, 162.

5 W. A. de Heer, *Rev. Mod. Phys.*, 1993, **65**, 611–676.

6 T. P. Martin, *Phys. Rep.*, 1996, **273**, 199–241.

7 U. Näher and K. Hansen, *J. Chem. Phys.*, 1994, **101**, 5367.

8 K. Hansen and U. Näher, *Phys. Rev. A*, 1999, **60**, 1240.

9 K. Hansen, *Statistical Physics of Nanoparticles in the Gas Phase*, Springer, Dordrecht, 2018, vol. 73.

10 F. Chandezon, S. Bjørnholm, J. Borggreen and K. Hansen, *Phys. Rev. B*, 1997, **55**, 5485.

11 J. Borggreen, K. Hansen, F. Chandezon, T. Døssing, M. Elhajal and O. Echt, *Phys. Rev. A*, 2000, **62**, 013202.

12 K. Hansen, P. Andersson and E. Uggerud, *J. Chem. Phys.*, 2009, **131**, 124303.

13 K. Hansen, M. Ryding and E. Uggerud, *Int. J. Mass Spectrom.*, 2019, **440**, 14–19.

14 S. Prasalovich, K. Hansen, M. Kjellberg, V. N. Popok and E. E. B. Campbell, *J. Chem. Phys.*, 2005, **123**, 084317.

15 M. Lippe, U. Szczepaniak, G.-L. Hou, S. Chakrabarty, J. J. Ferreiro, E. Chasovskikh and R. Signorell, *J. Phys. Chem. A*, 2019, **123**, 2426–2437.

16 B. Schläppi, J. H. Litman, J. J. Ferreiro, D. Stapfer and R. Signorell, *Phys. Chem. Chem. Phys.*, 2015, **17**, 25761.

17 J. J. Ferreiro, S. Chakrabarty, B. Schläppi and R. Signorell, *J. Chem. Phys.*, 2016, **145**, 211907.

18 O. Echt, K. Sattler and E. Recknagel, *Phys. Lett*, 1982, **90A**, 185–189.

19 J. Krohn, M. Lippe, C. Li and R. Signorell, *Phys. Chem. Chem. Phys.*, 2020, **22**, 15986–15998.

20 Y. Negishi, T. Nagata and T. Tsukuda, *Chem. Phys. Lett.*, 2002, **364**, 127–132.

21 O. Ingolfsson and A. M. Wodtke, *J. Chem. Phys.*, 2002, **117**, 3721.

22 O. Ingolfsson and A. M. Wodtke, *Chem. Phys. Lett.*, 2002, **360**, 415–421.

23 R. Halonen, V. Tikkanen, B. Reischl, K. K. Dingilian, B. E. Wyslouzil and H. Vehkamäki, *Phys. Chem. Chem. Phys.*, 2021, **23**, 4517–4529.

24 N. Bohr and J. A. Wheeler, *Phys. Rev.*, 1939, **57**, 426.

25 A. Bohr and B. R. Mottelson, *Nuclear Structure*, World Scientific, Singapore, 1998.

26 W. Saunders, *Phys. Rev. A*, 1992, **46**, 7028–7041.

27 M. Seidl and M. Brack, *Ann. Phys.*, 1996, **245**, 275–310.

28 U. Näher, S. Bjørnholm, S. Frauendorf, F. Garcias and C. Guet, *Physics Reports*, 1997, **285**, 245–320.

29 J. U. Andersen, E. Bonderup and K. Hansen, *J. Chem. Phys.*, 2001, **114**, 6518.

30 J. Gspann, *Z. Phys. D*, 1986, **3**, 143–145.

31 C. E. Klots, *J. Chem. Phys.*, 1988, **92**, 5864–5868.

32 K. Hansen, H. Hohmann, R. Müller and E. E. B. Campbell, *J. Chem. Phys.*, 1996, **105**, 6088.

33 C. E. Bryson, V. Cazcarra and L. L. Levenson, *J. Chem. Eng. Data*, 1974, **19**, 107–110.

34 W. Miehle, O. Kandler, T. Leisner and O. Echt, *J. Chem. Phys.*, 1989, **91**, 5940–5952.

35 T. P. Martin, U. Näher and H. Schaber, *Chem. Phys. Lett.*, 1992, **199**, 470–474.

36 L. Marks, *Philos. Mag. A*, 1984, **49**, 81–93.

37 C. L. Cleveland and U. Landman, *J. Chem. Phys.*, 1991, **94**, 7376–7396.

38 F. Baletto, R. Ferrando, A. Fortunelli, F. Montalenti and C. Mottet, *J. Chem. Phys.*, 2002, **116**, 3856–3863.

39 A. L. Garden, A. Pedersen and H. Jónsson, *Nanoscale*, 2018, **10**, 5124–5132.

40 U. Näher, U. Zimmermann and T. Martin, *J. Chem. Phys.*, 1993, **99**, 2256–2260.

41 G. Torchet, H. Bouchier, J. Farges, M. F. de Feraudy and B. Raoult, *J. Chem. Phys.*, 1984, **81**, 2137–2143.

42 D. Kreisle, O. Echt, M. Knapp and E. Recknagel, *Surf. Sci.*, 1985, **156**, 321–327.

43 O. Kandler, T. Leisner, O. Echt and E. Recknagel, *Z. Phys. D*, 1988, **10**, 295–301.

44 G. Torchet, M.-F. de Feraudy, A. Boutin and A. H. Fuchs, *J. Chem. Phys.*, 1996, **105**, 3671.

45 J.-B. Maillet, A. Boutin and A. H. Fuchs, *J. Chem. Phys.*, 1999, **111**, 2095.

46 M. A. Caprio, *Comput. Phys. Commun.*, 2005, **171**, 107.